The synergetic effect of cobalt content on enhancing the photoelectrochemical hydrogen production performance of in-*situ*-doped TiO₂ photocatalysts

A. N. El-Shazly [a,b,$], **A. H. Hegazy** [c,*,$], **M. A. Hamza** [b,d], **E. El Shenawy** [c], **N. K. Allam** [b,*]

[a] Central Metallurgical Research and Development Institute, P.O. Box 87, Helwan, Cairo, Egypt

[b] Energy Materials Laboratory, School of Sciences and Engineering, The American University in Cairo, New Cairo 11835, Egypt

[c] Solar Energy Department, National Research Centre, Giza, Dokki, Egypt

[d] Chemistry Department, Faculty of Science, Ain Shams University, Abbasia, Cairo, Egypt

* Corresponding author: E-mail: aiathussien@gmail.com, nageh.allam@aucegypt.edu, [$]equal contribution

Abstract

Pure TiO₂ nanoparticles (NPs) and cobalt-doped TiO₂ NPs with Co doping concentration up to 0.625 wt% were prepared by facile sol-gel technique onto FTO/glass substrates. The morphological, structural, and optical characteristics of the prepared nanoparticles were inspected by electron microscopy, X-ray diffraction, and spectroscopic techniques. The fabricated electrodes were used as photoanodes in photoelectrochemical cells (PEC) and their performance for water splitting was evaluated. The optimum doping concentration was 0.325 wt.%, which achieved an unprecedented improved photocurrent density of 10 mA/cm². Hence, this work reveals the promoting effect of Co ions on TiO₂ as promising photocatalysts for PEC water splitting with the tailoring of their electronic properties.

Keywords: Co-doped TiO₂; Oxygen vacancy; Photocatalysts; Water splitting; Solar energy.

1. Introduction

Water splitting has been recognized as one of the most efficient strategies to realize a sustainable energy conversion. Moreover, it provides a renewable, eco-friendly way for H₂ production [1,2]. Semiconductor-assisted photoelectrocatalysis is one of the outstanding low-cost strategies for water splitting [3–7]. Thus, many efforts have been dedicated to enhancing the photocatalytic performance of numerous semiconductors. TiO₂ was one of the most commonly investigated photocatalysts for PEC water splitting because of its low cost, non-toxicity, chemical stability, and photostability [8–12]. However, TiO₂-based photocatalysts have two main disadvantages; the large bandgap energy (3.2 eV) that restricts their photocatalytic efficiency to the UV region only, and their fast e-h recombination rates that decrease their photocatalytic efficiency [9,13,14]. To overcome these drawbacks, there are several approaches to enhance the photocatalytic performance of single-component photocatalysts, including semiconductor coupling with other materials [15–17],

dye sensitization [9,10,17], coupling with carbon materials [18,19], and doping [6,20]. As one of the efficient approaches to enhancing TiO₂ photocatalysts, doping with metals or non-metals could overcome the drawbacks of TiO₂ by decreasing its bandgap energy and decreasing the e-h recombination [21–27]. Thus, co-doping of two or more metal/non-metal atoms/ions, e.g. (C, N, & Fe) or (Cu, Co, Ni, & Ti³⁺) showed better synergistic effects and overcame the drawbacks of single dopants [28–30]. Also, CoOₓ is one of the efficient co-catalysts, exhibiting a band alignment with the TiO₂ signifying their ability to enhance the charge separation, reduce the bandgap energy, and provide more active sites [31]. Besides, carbon doping or coupling with organic showed a remarkable enhancement in the conductivity of TiO₂, as it is capable of improving the charge transfer from the bulk to the surface of titanium dioxide, and the required redox reactions occur [18,32]. For this purpose, metal-doped TiO₂ nanoparticles have gained concerns as an

efficient photocatalyst compared to undoped counterparts. Herein, we demonstrate the influence of the amount of incorporated cobalt in TiO_2 *via* a simple sequence of sol-gel method and topotactic transformations. The characteristics of the synthesized TiO_2-xCo nanoparticles were explored by FE-SEM, HR-TEM, XRD, FTIR, DRS, PL, and Raman spectra. In addition, to explore the visible-light-driven PEC performance, thin films of the fabricated pure and Co-doped TiO_2 samples were fabricated by drop-casting on FTO to act as photoanodes in the PEC cell to study the synergetic effect of cobalt-doping with other dopants. All the experimental details, including materials synthesis, physicochemical characterizations, and PEC characterizations, are stated in the supporting information file.

2. Experimental

See the supplemental file for detailed description of materials, nanoparticles preparation, and characterization.

3. Results and discussions

3.1. Physicochemical characterizations

The surface microstructure and morphology of the as-prepared pure TiO_2 and TiO_2-xCo NPs were investigated by FESEM, as illustrated in **Fig. 1(a–e)**. In the absence of Co dopants, the morphologies of the obtained undoped TiO_2 NPs were dense structures with flakes emerging from the surface.
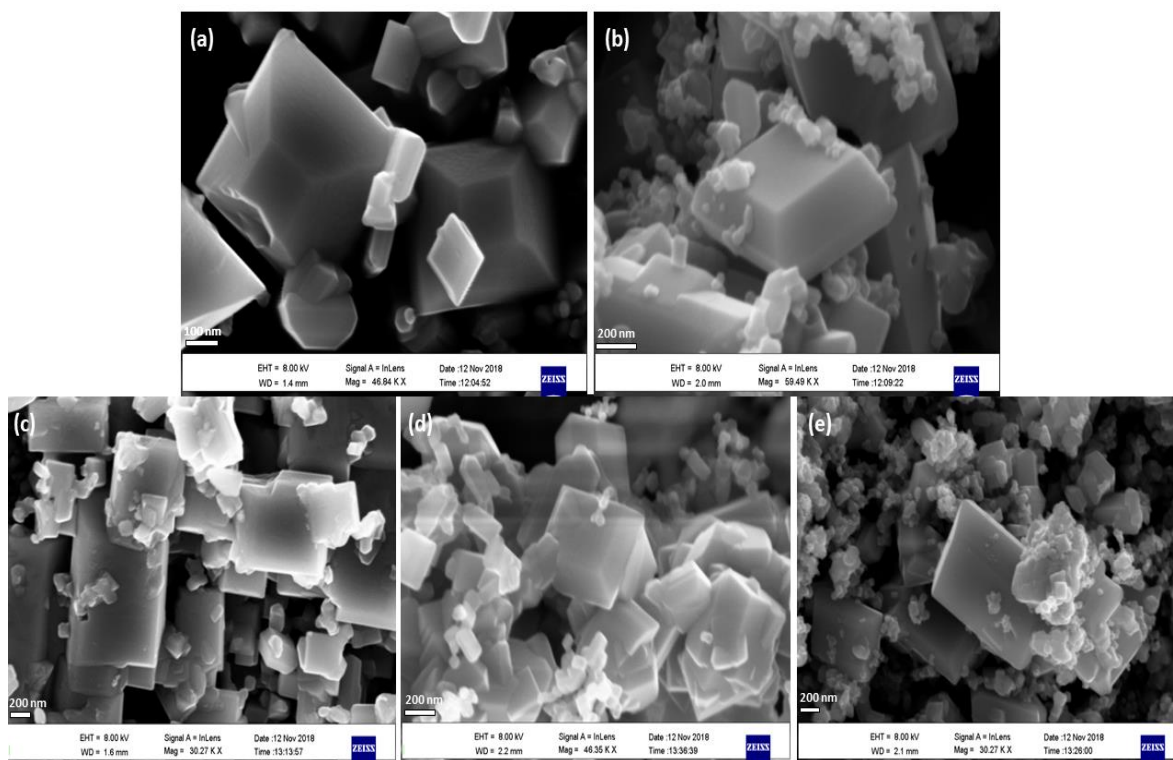

Fig. 1 FE-SEM images of (a) pure TiO_2, (b-e) TiO_2-XCo NPs (where X=0.125, 0.25, 0.325 and 0.625), respectively.

However, a closer examination revealed a large number of rhombohedral structures along with the smooth surface of the nanoparticles, indicating in-situ crystallization of the formed structures [33]. No drastic change in the microstructure was observed upon Co doping with different proportions. HR-TEM micrographs and EDX analysis of pure TiO_2 and TiO_2-xCo NPs (**Fig. 2a-f**) reveal a square surface of highly crystalline anatase TiO_2 with the characteristic {001} facets. As mentioned in the lower inset of **Fig. 2a**,

pure TiO_2 shows the lattice d-spacing of 0.12 nm, which is characteristic of the (101) plane of the tetragonal anatase TiO_2 phase [34]. In addition, the related electron diffraction rings (SAED) (upper inset of Fig. 2a) suggested the existence of polycrystals [35]. Moreover, the same morphology is kept after the addition of cobalt, **Fig. 2(b-e)**. In addition, the EDX is an excellent tool for the quantitative identification of elements in the synthesized nanoparticles as well as the concentration of dopants (**Fig. 2f**).

EDX confirmed the presence of cobalt (Co) with wt. % of 0.11, 0.27, 0.36, and 0.62% for TiO_2-0.125Co, TiO_2-0.25Co, TiO_2-0.325Co, and TiO_2- 0.625Co, respectively. Besides, Titanium (Ti) and Oxygen (O) peaks that originate from the TiO_2 precursors were also evident.

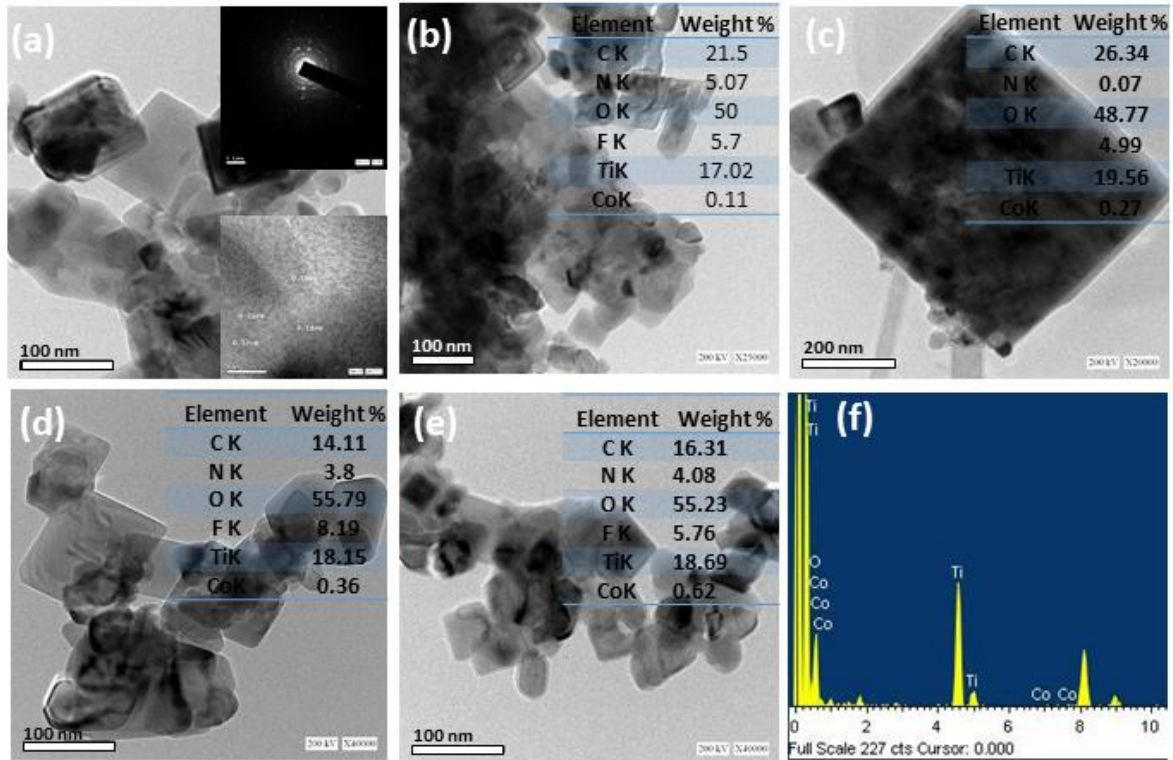**Fig. 2** HR-TEM images of (a) pure TiO_2, (b-e) TiO_2-XCo NPs (where X=0.125, 0.25, 0.325 and 0.625), respectively

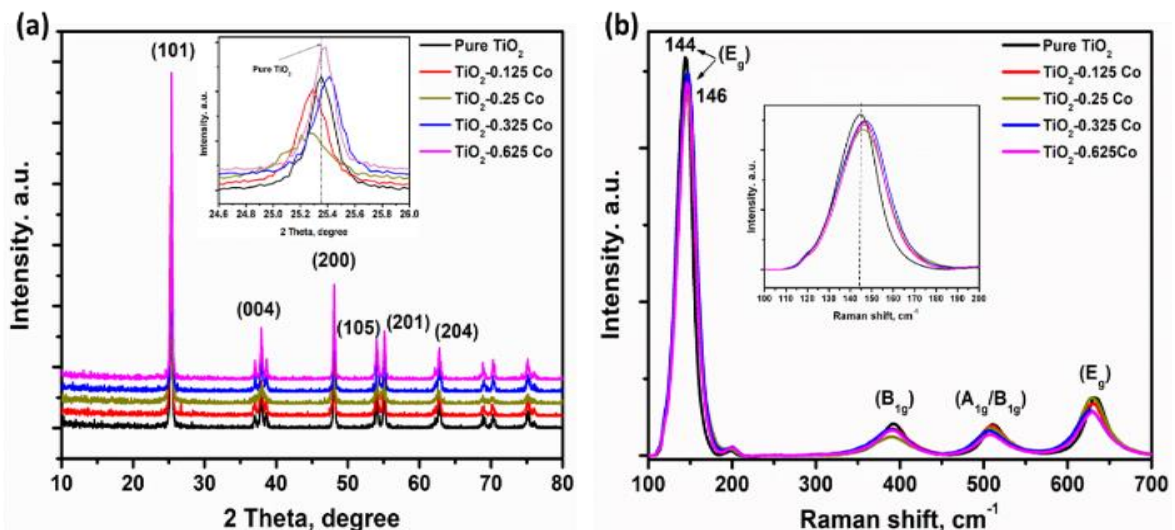**Fig. 3** (a) PXRD patterns, and (b) Raman spectra of the pure TiO_2 and TiO_2-XCo NPs (where X=0.125, 0.25, 0.325 and 0.625), respectively.

Figure 3a illustrates the PXRD patterns of pure TiO_2 NPs and the patterns of the Co-doped TiO_2 NPs with different doping concentrations. All samples reveal sharp, narrow, and well crystalline distinctive peaks of the TiO_2 anatase phase (JCPDS 78-2486) [36]. No characteristic peaks of cobalt oxide or metallic cobalt

were detected because of the low concentrations of Co, which are less than the detection limit of PXRD [37]. The inset of **Fig. 3a** shows the details of the strongest diffraction peak of (101), which is shifted toward a lower angle for low doping concentration (0.125 and 0.25 wt. % of Co) and to a higher angle for high doping concentration (0.325 and 0.625 wt. % of Co), providing the change in the lattice parameters of TiO$_2$ local structure and the successful doping of cobalt. As the Co atom has a different size than Ti, substituting Co at Ti sites either by low or high percent will create Ti interstitials or vacancies, oxygen vacancies, impurities, and defects at interfaces to balance the charge neutrality [38]. The local structure change in the Co-doped TiO$_2$ NPs was elucidated via Raman spectroscopy, see **Fig. 3b**. The typical 6 Raman-active bands (3 E$_g$ + 2B$_{1g}$ + A$_{1g}$) of the anatase phase were detected. Besides, the bands appeared at about 144, 196, and 632 cm^{-1} for E$_g$ modes [39], corresponding to the symmetric stretching vibration of O-Ti-O; Raman bands at 392 and 511 cm^{-1} for 2B$_{1g}$ are characteristic of the symmetric bending vibration of O–Ti–O, and the A$_{1g}$ mode at 512 cm^{-1} could be correlated to asymmetric bending vibration of O–Ti–O. Nevertheless, Co-doped TiO$_2$ samples showed the same six distinctive Raman vibration modes but with a little shift, suggesting anatase TiO$_2$ structure was not destroyed by doping at low or high concentrations. We could also differentiate between the samples from the Raman spectra. More clearly, the position and FWHM of the peak at 143.02 cm^{-1} (Eg mode) are evident that cobalt is successfully doped into TiO$_2$, as listed in **Table 1.** Therefore, the reason behind the broadening and shifts of the Raman peaks is the effect of the particle size that may affect the frequency because of the electron-phonon coupling and oxygen vacancies. The accumulated strains in the doped semiconductors can change the linewidth and the shape of the peaks in the Raman spectra and decreases the phonon lifetime, as shown in **Table 1**.

The phonon lifetime (τ) was estimated from the Lorentzian-fitted phonon modes by using the relation of energy-time uncertainty (**Eq. 1**) [40]:

$$1/\tau = \Delta E/h = 2\pi c r \qquad (1)$$

Figure 4 depicts the FTIR spectra; the broad bands located at 3435 and 3750 cm^{-1} can be attributed to the stretching vibrations caused by the adsorption of O-H on the different facets of the TiO$_2$ NPs [41]. The peaks at 1643 cm^{-1} are the typical bending modes of water molecules. The band located at 1427 cm^{-1} could be ascribed to the vibrations of the Ti-O bond [42].

Table. 1 The experimental weight % concentrations of cobalt doping, full width at half maximum (FWHM), phonon lifetime, and calculated bandgaps of pure TiO$_2$ and TiO$_2$-XCo NPs (where X=0.125, 0.25, 0.325, and 0.625).

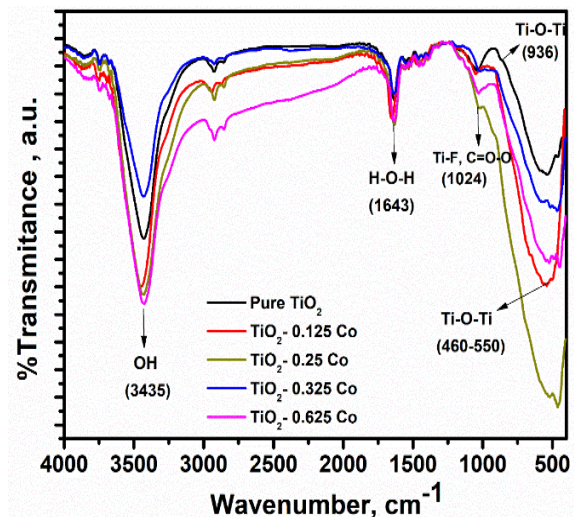| Concentration of Co^{2+}, wt.%	FWHM, cm^{-1}	Lifetime, s (× 10^{-13})	Bandgap, eV
0	21.29	2.49	2.75
0.125	25.13	2.11	2.67
0.25	26.88	1.97	2.58
0.325	26.78	1.98	2.3
0.625	23.95	2.21	2.87

Fig. 4 FTIR spectra of the pure TiO$_2$ and TiO$_2$-XCo NPs (where X=0.125, 0.25, 0.325 and 0.625), respectively.

Moreover, at 1024 cm^{-1}, the band also was from the Ti-F vibrations. Finally, the band centered between 521 and 460 cm^{-1} was accredited to the Ti-O vibrations, as this band was observed in all samples of pure TiO$_2$ and the Co-doped samples. Notably, a small shift in the spectra of the Co-doped samples was seen, which confirms the cobalt doping in TiO$_2$ lattice.

As represented in **Fig. 5a**, the Tauc plot reveals the calculated bandgap of all samples. The observed bandgap of the pure and TiO$_2$-xCo NPs are listed in **Table 1**. The Co-doped TiO$_2$ NPs samples displayed a red-shift compared to the pure TiO$_2$ NPs (2.75 eV). TiO$_2$ is an n-type semiconductor exhibiting natural electron donors produced by Ti interstitials and O vacancies. Incorporating acceptor Co ions can shift the Fermi level towards the CB [43]. This bandgap

reduction is attributed to defect states below the CB, which originate from the $Co^{2+} \rightarrow Ti^{4+}$ charge-transfer interaction. Notably, with a further increase in the dopant concentration, the bandgap increased for TiO_2-0.625Co as the high number of defects appeared on the TiO_2 surface and increased the electron transition barrier; thus, the bandgap changed [44].

Fig. 5b displays the PL spectra of the synthesized pure TiO_2 and TiO_2-xCo NPs between 300 nm and 900 nm. Note that pure TiO_2 and TiO_2-xCo NPs have no different emission peaks. Moreover, the PL intensity of all TiO_2-xCo NPs is less than that of pure TiO_2 NPs. These findings confirm the successful doping of Co into TiO_2 lattice. They indicate that the recombination of photoinduced e-h pairs has been efficiently suppressed by this method of cobalt doping, (i) low-intensity peak at 396 nm is consistent with the ultra-violet (UV) region and could be correlated to the emission of TiO_2 bandgap transition, (ii) broad peaks centered at 423 nm are representative of the violet region, which is related to the self-trapping excitons, (iii) other peaks centered at 441, 453, 469, 481, and 491 nm correspond to the presence of oxygen vacancies or defects, (iv) high-intensity peak at 530 - 680 nm corresponds to the green band. Moreover, the sharp peak at 825 nm represents the red region and supposed to be a result of the recombination from the defect states of Ti^{3+} to the VB. The above results indicate that the recombination of photogenerated e-h pairs is effectively suppressed upon cobalt doping. These findings suggest that the TiO_2-xCo NPs will display improved photocatalytic performance than that of the undoped TiO_2 NPs.

3.2. Photoelectrochemical characterization

To get insights into the effects of cobalt doping on the photoelectrochemical behavior of the fabricated TiO_2 NPs, various TiO_2-xCo electrodes were fabricated and examined under AM1.5 illuminations as a solar simulator. The J–V plots are collected in 1 M KOH, as shown in **Fig. 6.** The concentration of the cobalt doping on TiO_2 presented a significant influence on the photocurrent density. For instance, the electrode with 0.125 wt.% Co (TiO_2-0.125Co) demonstrated an increase in the photocurrent density (5.7 mA cm^{-2}) that is higher than the recorded photocurrent density of the as-fabricated TiO_2 (4.4 mA cm^{-2}).

Increasing the wt.% of cobalt doping to (0.25, 0.325, and 0.625) causes a substantial increase in the photocurrent density, reaching its highest value for the

electrodes with 0.325% Co of 10 mA cm^{-2}, which is 2.5-fold greater than that obtained for the pure TiO_2 electrode, after which in TiO_2-0.625Co electrodes, the photocurrent density curve recorded a remarkable drop, implying the optimal doping concentration of 0.325%. This might be due to excessive Co doping, which may block the light photons reaching the electrode surface and cause a bad interfacial contact between TiO_2-0.625Co NPs and FTO electrodes [45]. Therefore, the extremely high photocurrent densities of the TiO_2-xCo NPs electrodes indicate the positive influence of Co doping that created predominant shallow defects, improving the photoelectrochemical water splitting performance compared to the pure TiO_2 NPs. However, deep defects were created upon increasing doping concentration and reduced the charge transfer of the photoinduced charge carriers in TiO_2-0.625Co NPs, as proposed by the PL findings [46].

Furthermore, To thoroughly explain the photocurrent enhancement in TiO_2-xCo NPs , Mott-Schottky analysis of the obtained EIS was used for the estimation of the density of charge carriers (N_D) of the synthesized photoanodes, according to Eq. (2) [47].

$$N_D = -\left[\frac{2}{\varepsilon\varepsilon_o e}\right]\left[\frac{d\left(\frac{1}{C^2}\right)}{d(V)}\right]^{-1} \qquad (2)$$

where N_D is the donor density, ε is the dielectric constant, ε_o is the permittivity in free space, e is the charge of the electron, C is the space charge capacitance, and V is the voltage applied.

The N_D values of pure TiO_2, TiO_2-0.125Co, TiO_2-0.25Co, TiO_2-0.325Co and TiO_2-0.625Co samples were calculated as 3.27×10^{18} cm^{-3}, 10.04×10^{18} cm^{-3}, 32.05×10^{24} cm^{-3}, 89.96×10^{18} cm^{-3}, and 46.76×10^{18} cm^{-3}, respectively. Thus, it is clear that the donor density of the TiO_2 is increased after doping with cobalt.

The increased donor density in the TiO_2-xCo NPs can be ascribed to the characteristic carrier density exhibited by cobalt, as suggested in the Mott-Schottky analysis. The carrier concentrations decreased after incorporating a high percentage of cobalt in TiO_2-0.625Co NPs. It reveals that doping with transition metal ions like Co is an efficient strategy to increase the donor densities of TiO_2 NPs. Hence, the improved photocurrents are ascribed to the boosted donor densities that are supposed to move the Fermi level of TiO_2 near the CB and smooth the charge separation by increasing the band bending.
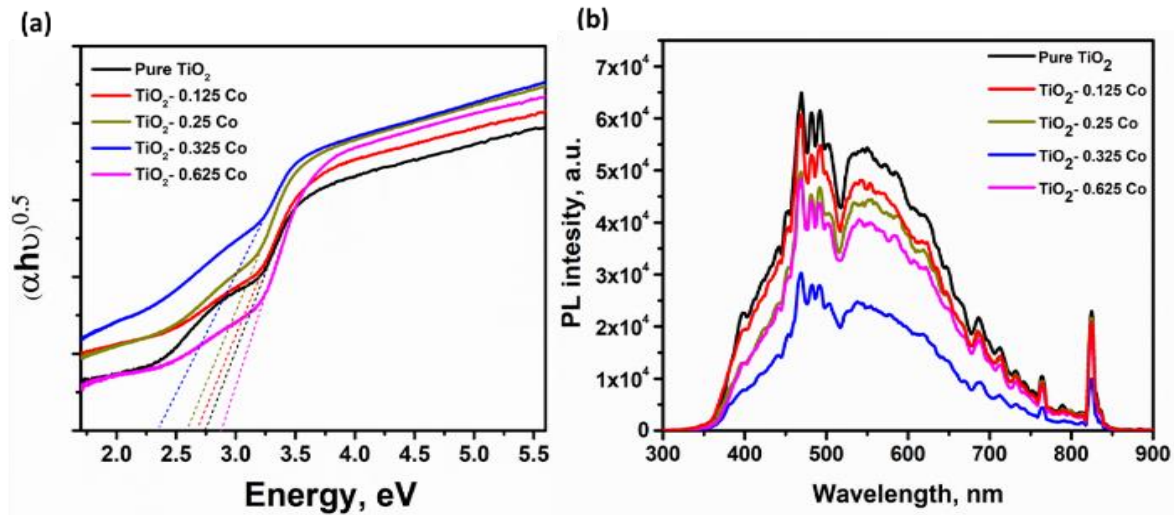
Fig. 5 (a) Tauc plot, and (b) PL spectra of the pure TiO_2 and TiO_2-XCo NPs (where X=0.125, 0.25, 0.325 and 0.625), respectively.

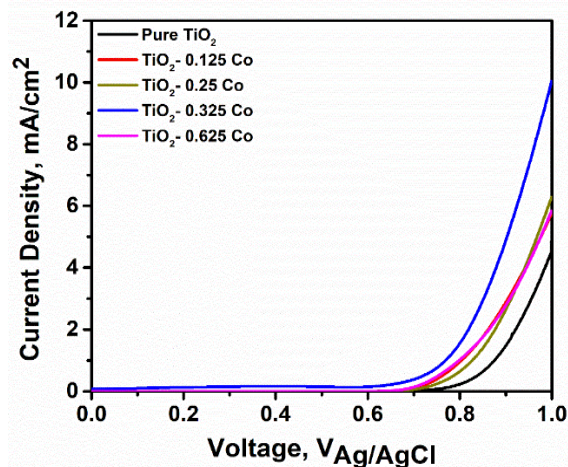**Fig. 6** The photoelectrochemical performance of the pure TiO_2 and TiO_2-XCo NPs (where X=0.125, 0.25, 0.325, and 0.625), respectively.

4. Conclusion

In summary, we demonstrated the successful preparation of TiO_2-xCo NPs *via* the facile sol-gel route followed by topotactic transformations. The novel fabrication method is very handy and allowed us to fabricate the material in various compositions with x varying from 0.125 to 0.625. The as-synthesized materials were found to be in-situ crystallized during synthesis. The Raman analysis revealed the anatase phase formation of all synthesized materials. Moreover, scanning and transmission electron microscopy findings revealed uniform and homogeneous structures. Optical properties analysis demonstrated a decrease in the optical bandgap from 2.75 to 2.3 at x = 0.325. All compositions of the fabricated TiO_2-xCo NPs were evaluated as photoanodes for PEC water splitting, where the highest current density of 10 mA/cm² of the TiO_2-0.325Co NPs under simulated solar irradiation achieved a high electron carrier density of 89.96 × 10^{18} cm⁻³, which are the highest values ever achieved for TiO_2-based photoelectrodes. Finally, this report indicates that TiO_2-xCo NPs hold promise for PEC water splitting and other solar energy-based applications.

Acknowledgments

References

[1] B. Tan, X. Zhang, Y. Li, H. Chen, X. Ye, Y. Wang, J. Ye, Anatase TiO_2 Mesocrystals: Green Synthesis, In Situ Conversion to Porous Single Crystals, and Self-Doping Ti^{3+} for Enhanced Visible Light Driven Photocatalytic Removal of NO, Chem. - A Eur. J. 23 (2017) 5478–5487. https://doi.org/10.1002/chem.201605294.

[2] A. Fujishima, K. Honda, Electrochemical Photolysis of Water at a Semiconductor Electrode, Nature. 238 (1972) 37–38. https://doi.org/10.1038/238037a0.

[3] M.A. Hamza, A.N. El-Shazly, S.A. Tolba, N.K. Allam, Novel Bi-based photocatalysts with unprecedented visible light-driven hydrogen production rate: Experimental and DFT insights, Chem. Eng. J. 384 (2020) 123351. https://doi.org/10.1016/j.cej.2019.123351.

[4] A.N. El-Shazly, M.A. Hamza, N.K. Allam, Enhanced photoelectrochemical water splitting via engineered surface defects of $BiPO_4$ nanorod photoanodes, Int. J. Hydrogen Energy. 46 (2021) 23214–23224.
https://doi.org/10.1016/j.ijhydene.2021.04.134.

[5] A.N. El-Shazly, A.H. Hegazy, M.M. Rashad, M.F. El-Shahat, N.K. Allam, Ultrathin ALD TiO_2 shells for enhanced photoelectrochemical solar fuel generation, J. Alloys Compd. 739 (2018). https://doi.org/10.1016/j.jallcom.2017.12.218.

[6] A.N. El-Shazly, A.H. Hegazy, E.T. El Shenawy, M.A. Hamza, N.K. Allam, Novel facet-engineered multi-doped TiO_2 mesocrystals with unprecedented visible light photocatalytic hydrogen production, Sol. Energy Mater. Sol. Cells. 220 (2021) 110825. https://doi.org/10.1016/j.solmat.2020.110825.

[7] M.A. Hamza, A.N. El-Shazly, N.K. Allam, Facile template-free one-pot room-temperature synthesis of novel m-Bi(OH)CrO₄ microspheres, Mater. Lett. 262 (2020) 127188. https://doi.org/10.1016/j.matlet.2019.127188.

[8] C. Liu, F. Wang, S. Zhu, Y. Xu, Q. Liang, Z. Chen, Controlled charge-dynamics in cobalt-doped TiO_2 nanowire photoanodes for enhanced photoelectrochemical water splitting, J. Colloid Interface Sci. 530 (2018) 403–411. https://doi.org/10.1016/j.jcis.2018.07.003.

[9] M.A. Hamza, Z.M. Abou-Gamra, M.A. Ahmed, The critical role of Tween 80 as a 'green' template on the physical properties and photocatalytic performance of -TiO_2 nanoparticles for Rhodamine B photodegradation, J. Mater. Sci. Mater. Electron. (2020). https://doi.org/10.1007/s10854-020-03017-2.

[10] M.A. Ahmed, Z.M. Abou-Gamra, H.A.A. Medien, M.A. Hamza, Effect of porphyrin on photocatalytic activity of TiO_2 nanoparticles toward Rhodamine B photodegradation, J. Photochem. Photobiol. B Biol. 176 (2017) 25–35. https://doi.org/10.1016/j.jphotobiol.2017.09.016.

[11] A. Hegazy, E. El-Shenawy, M. Abdelatef, Decoupling crystallinity and size of TiO_2 Nanoparticles of TiO_2: Application in large area dye-sensitized solar cells, ISES Sol. World Congr. 2017 - IEA SHC Int. Conf. Sol. Heat. Cool. Build. Ind. 2017, Proc. (2017) 1240–1250. https://doi.org/10.18086/swc.2017.20.05.

[12] A. Hegazy, High performance crystalline TiO_2 mesocrystals for enhanced solar fuel, Egypt. J. Chem. 62 (2019) 115–122. https://doi.org/10.21608/EJCHEM.2019.13610.1841.

[13] S.G. Kumar, L.G. Devi, Review on modified TiO_2 photocatalysis under UV/visible light: Selected results and related mechanisms on interfacial charge carrier transfer dynamics, J. Phys. Chem. A. 115 (2011) 13211–13241. https://doi.org/10.1021/jp204364a.

[14] A. Hegazy, E. Prouzet, Effect of physical chemistry parameters in photocatalytic properties of TiO_2 nanocrystals, Comptes Rendus Chim. 16 (2013) 651–659. https://doi.org/10.1016/j.crci.2013.04.008.

[15] M.A. Hamza, S.A. Abd El-Rahman, Z.M. Abou-Gamra, Facile one-pot solid-state fabrication of a novel binary nanocomposite of commercial ZnO and commercial $PbCrO_4$ with enhanced photocatalytic degradation of Rhodamine B dye, Opt. Mater. (Amst). 124 (2022) 111987. https://doi.org/10.1016/j.optmat.2022.111987.

[16] H. Hou, L. Wang, F. Gao, X. Yang, W. Yang, $BiVO_4$@TiO_2 core-shell hybrid mesoporous nanofibers towards efficient visible-light-driven photocatalytic hydrogen production, J. Mater. Chem. C. 7 (2019) 7858–7864. https://doi.org/10.1039/c9tc02480h.

[17] H. Ding, M. Xu, S. Zhang, F. Yu, K. Kong, Z. Shen, J. Hua, Organic blue-colored D-A-π-A dye-sensitized TiO_2 for efficient and stable photocatalytic hydrogen evolution under visible/near-infrared-light irradiation, Renew. Energy. 155 (2020) 1051–1059. https://doi.org/10.1016/j.renene.2020.04.009.

[18] A.M. Ismael, A.N. El-Shazly, S.E. Gaber, M.M. Rashad, A.H. Kamel, S.S.M. Hassan, Novel TiO_2/GO/$CuFe_2O_4$ nanocomposite: a magnetic, reusable and visible-light-driven photocatalyst for efficient photocatalytic removal of chlorinated pesticides from wastewater, RSC Adv. 10 (2020) 34806–34814. https://doi.org/10.1039/d0ra02874f.

[19] M.A. Hamza, S.A. Abd El-Rahman, A.N. El-Shazly, E.M. Hashem, R.T. Mohamed, E.M. El-

Tanany, M.G. Elmahgary, Facile one-pot ultrasonic-assisted synthesis of novel Ag@RGO/g-C$_3$N$_4$ ternary 0D@2D/2D nanocomposite with enhanced synergetic tandem adsorption-photocatalytic degradation of recalcitrant organic dyes: Kinetic and mechanistic insights, Mater. Res. Bull. 142 (2021) 111386. https://doi.org/10.1016/j.materresbull.2021.1113 86.

[20] B. Liu, H.M. Chen, C. Liu, S.C. Andrews, C. Hahn, P. Yang, Large-scale synthesis of transition-metal-doped TiO$_2$ nanowires with controllable overpotential, J. Am. Chem. Soc. 135 (2013) 9995–9998. https://doi.org/10.1021/ja403761s.

[21] J. Yu, G. Dai, Q. Xiang, M. Jaroniec, Fabrication and enhanced visible-light photocatalytic activity of carbon self-doped TiO$_2$ sheets with exposed {001} facets, J. Mater. Chem. 21 (2011) 1049–1057. https://doi.org/10.1039/c0jm02217a.

[22] S.U.M. Khan, M. Al-Shahry, W.B. Ingler, Efficient photochemical water splitting by a chemically modified n-TiO$_2$, Science 297 (2002) 2243–2245.
https://doi.org/10.1126/science.1075035.

[23] M.S. Lee, S.S. Hong, M. Mohseni, Synthesis of photocatalytic nanosized TiO$_2$-Ag particles with sol-gel method using reduction agent, J. Mol. Catal. A Chem. 242 (2005) 135–140. https://doi.org/10.1016/j.molcata.2005.07.038.

[24] S. Kim, S.J. Hwang, W. Choi, Visible light active platinum-ion-doped TiO$_2$ photocatalyst, J. Phys. Chem. B. 109 (2005) 24260–24267. https://doi.org/10.1021/jp055278y.

[25] D.H. Kim, K. Sub Lee, Y.S. Kim, Y.C. Chung, S.J. Kim, Photocatalytic activity of Ni 8 wt%-doped TiO$_2$ photocatalyst synthesized by mechanical alloying under visible light, J. Am. Ceram. Soc. 89 (2006) 515–518. https://doi.org/10.1111/j.1551-2916.2005.00782.x.

[26] U.G. Akpan, B.H. Hameed, The advancements in sol-gel method of doped-TiO$_2$ photocatalysts, Appl. Catal. A Gen. 375 (2010) 1–11. https://doi.org/10.1016/j.apcata.2009.12.023.

[27] X. Tang, D. Li, Sulfur-doped highly ordered TiO$_2$ nanotubular arrays with visible light response, J. Phys. Chem. C. 112 (2008) 5405–5409. https://doi.org/10.1021/jp710468a.

[28] I. V. Baklanova, V.P. Zhukov, V.N. Krasil'nikov, O.I. Gyrdasova, L.Y. Buldakova, E. V. Shalaeva, E. V. Polyakov, M. V. Kuznetsov, I.R. Shein,

E.G. Vovkotrub, Fe and C doped TiO2 with different aggregate architecture: Synthesis, optical, spectral and photocatalytic properties, first-principle calculation, J. Phys. Chem. Solids. 111 (2017) 473–486. https://doi.org/10.1016/j.jpcs.2017.08.024.

[29] M.M. Hasan, S.A. Tolba, N.K. Allam, In Situ Formation of Graphene Stabilizes Zero-Valent Copper Nanoparticles and Significantly Enhances the Efficiency of Photocatalytic Water Splitting, ACS Sustain. Chem. Eng. 6 (2018) 16876–16885.
https://doi.org/10.1021/acssuschemeng.8b04219.

[30] X. Yu, X. Fan, L. An, Z. Li, J. Liu, Facile synthesis of Ti^{3+}-TiO$_2$ mesocrystals for efficient visible-light photocatalysis, J. Phys. Chem. Solids. 119 (2018) 94–99. https://doi.org/10.1016/j.jpcs.2018.03.024.

[31] M.A. Khan, M. Al-Oufi, A. Tossef, Y. Al-Salik, H. Idriss, On the role of CoO in CoO$_x$/TiO$_2$ for the photocatalytic hydrogen production from water in the presence of glycerol, Catal. Struct. React. 1 (2015) 192–200. https://doi.org/10.1080/2055074X.2015.1124191.

[32] Q. Zhang, N. Bao, X. Wang, X. Hu, X. Miao, M. Chaker, D. Ma, Advanced Fabrication of Chemically Bonded Graphene/TiO$_2$ Continuous Fibers with Enhanced Broadband Photocatalytic Properties and Involved Mechanisms Exploration, Sci. Rep. 6 (2016) 1–15. https://doi.org/10.1038/srep38066.

[33] L. Bahrig, S.G. Hickey, A. Eychmüller, Mesocrystalline materials and the involvement of oriented attachment-a review, CrystEngComm. 16(2014)9408–9424.
https://doi.org/10.1039/c4ce00882k.

[34] Y. Liu, Y.E. Du, Y. Bai, J. An, J. Li, X. Yang, Q. Feng, Facile Synthesis of {101}, {010} and [111]-Faceted Anatase-TiO$_2$ Nanocrystals Derived from Porous Metatitanic Acid H$_2$TiO$_3$ for Enhanced Photocatalytic Performance, ChemistrySelect. 3 (2018) 2867–2876. https://doi.org/10.1002/slct.201800018.

[35] S. Dai, Y. Wu, T. Sakai, Z. Du, H. Sakai, M. Abe, Preparation of highly crystalline TiO$_2$ nanostructures by acid-assisted hydrothermal treatment of hexagonal-structured nanocrystalline titania/cetyltrimethyammonium bromide nanoskeleton, Nanoscale Res. Lett. 5 (2010)1829–1835.
https://doi.org/10.1007/s11671-010-9720-0.

[36] E. V. Salomatina, A.S. Loginova, S. Ignatov, A.

V. Knyazev, I. V. Spirina, L.A. Smirnova, Structure and Catalytic Activity of Poly(Titanium Oxide) Doped by Gold Nanoparticles in Organic Polymeric Matrix, J. Inorg. Organomet. Polym. Mater. 26 (2016) 1280–1291. https://doi.org/10.1007/s10904-016-0409-4.

[37] W.F. Chen, P. Koshy, Y. Huang, E. Adabifiroozjaei, Y. Yao, C.C. Sorrell, Effects of precipitation, liquid formation, and intervalence charge transfer on the properties and photocatalytic performance of cobalt- or vanadium-doped TiO_2 thin films, Int. J. Hydrogen Energy. (2016) 19025–19056. https://doi.org/10.1016/j.ijhydene.2016.08.115.

[38] A.M. Elbanna, K.E. Salem, A.M. Mokhtar, M. Ramadan, M. Elgamal, H. A. Motaweh, H. M. Tourk, M. A-H. Gepreel, N. K. Allam, Ternary Ti–Mo–Fe Nanotubes as Efficient Photoanodes for Solar-Assisted Water Splitting, J. Phys. Chem. C (2021) 125, 12504–12517. https://doi.org/10.1021/acs.jpcc.1c01478

[39] A. Orendorz, A. Brodyanski, J. Lösch, L.H. Bai, Z.H. Chen, Y.K. Le, C. Ziegler, H. Gnaser, Phase transformation and particle growth in nanocrystalline anatase TiO_2 films analyzed by X-ray diffraction and Raman spectroscopy, Surf. Sci. 601 (2007) 4390–4394. https://doi.org/10.1016/j.susc.2007.04.127.

[40] S.S. Mali, C.A. Betty, P.N. Bhosale, P.S. Patil, Hydrothermal synthesis of rutile TiO_2 with hierarchical microspheres and their characterization, CrystEngComm. 13 (2011) 6349–6351. https://doi.org/10.1039/c1ce05928a.

[41] A.N. El-Shazly, G.S. El-Sayyad, A.H. Hegazy, M.A. Hamza, R.M. Fathy, E.T. El Shenawy, N.K. Allam, Superior visible light antimicrobial performance of facet engineered cobalt doped TiO_2 mesocrystals in pathogenic bacterium and fungi, Sci. Rep. 11 (2021) 1–14. https://doi.org/10.1038/s41598-021-84989-x.

[42] Y. Zhang, Q. Zhang, T. Xia, D. Zhu, Y. Chen, X. Chen, The Influence of Reaction Temperature on the Formation and Photocatalytic Hydrogen Generation of (001) Faceted TiO_2 Nanosheets, ChemNanoMat. 1 (2015) 270–275. https://doi.org/10.1002/cnma.201500030.

[43] X. Li, Z. Guo, T. He, The doping mechanism of Cr into TiO_2 and its influence on the photocatalytic performance, Phys. Chem. Chem. Phys. 15 (2013) 20037–20045. https://doi.org/10.1039/c3cp53531b.

[44] M. Liu, Q. Zhan, W. Li, R. Li, Q. He, Y. Wang, Effect of Zn doping concentration on optical band gap of PbS thin films, J. Alloys Compd. 792 (2019) 1000–1007. https://doi.org/10.1016/j.jallcom.2019.04.117.

[45] P. Sudhagar, T. Song, A. Devadoss, J.W. Lee, M. Haro, C. Terashima, V. V. Lysak, J. Bisquert, A. Fujishima, S. Gimenez, U. Paik, Modulating the interaction between gold and TiO_2 nanowires for enhanced solar driven photoelectrocatalytic hydrogen generation, Phys. Chem. Chem. Phys. 17 (2015) 19371–19378. https://doi.org/10.1039/c5cp01175b.

[46] A. El-Sayed, N. Atef, A.H. Hegazy, K.R. Mahmoud, R.M.A. Hameed, N.K. Allam, Defect states determined the performance of dopant-free anatase nanocrystals in solar fuel cells, Sol. Energy. 144 (2017) 445–452. https://doi.org/10.1016/j.solener.2017.01.056.

[47] B. Chen, B. Ge, S. Fu, Q. Li, X. Chen, L. Li, J. Wang, Z. Yang, J. Ding, W. Fan, B. Mao, W. Shi, Ex-situ flame co-doping of tin and tungsten ions in TiO_2 nanorod arrays for synergistic promotion of solar water splitting, Chem. Eng. Sci. 226 (2020). https://doi.org/10.1016/j.ces.2020.115843.